

Impact of Hot Inner Crust on The Properties of Hot Compact Stars

Clara Dehman,^{1,2,3*} Mario Centelles,^{4,5} and Xavier Viñas^{4,5,6}

¹ Institute of Space Sciences (ICE-CSIC), Campus UAB, Carrer de Can Magrans s/n, 08193, Barcelona, Spain

² Institut d'Estudis Espacials de Catalunya (IEEC), Carrer Gran Capità 2–4, 08034 Barcelona, Spain

³ Nordita, KTH Royal Institute of Technology and Stockholm University, 10691 Stockholm, Sweden

⁴ Departament de Física Quàntica i Astrofísica (FQA), Universitat de Barcelona (UB), Martí i Franquès 1, 08028 Barcelona, Spain

⁵ Institut de Ciències del Cosmos (ICCUB), Universitat de Barcelona (UB), Martí i Franquès 1, 08028 Barcelona, Spain

⁶ Institut Menorquí d'Estudis, Camí des Castell 28, 07702 Maó, Spain

ABSTRACT

We have conducted a study on the thermal properties of the recently developed nuclear energy density functional known as BCPM. This functional is founded on microscopic calculations that incorporate the realistic Argonne v_{18} potential along with Urbana-type three-body forces. BCPM has demonstrated success in describing finite nuclei and cold neutron stars. However, investigating the properties of hot β -stable matter under both neutrino-free and neutrino-trapped scenarios is vital for astrophysical applications. In this study, we investigate the BCPM equation of state for β -stable, neutrino-free matter at finite temperatures, taking into consideration the hot inner crust and applying the frozen correlation approximation. Such an equation of state holds significant importance for hot compact objects, such as the final result of a binary neutron star merger event. Our exploration has unveiled the presence of cluster regions, persisting up to a temperature of approximately 7.2 MeV, denoted as the limiting temperature. Beyond this limiting temperature, clusters are not anticipated to manifest. At temperatures below the limiting threshold, clusters within the inner crust are encompassed by uniform matter with varying densities, facilitating the distinction between the higher and lower transition density branches. Furthermore, we have computed mass-radius relationship, while assuming an isothermal profile for neutron star matter at diverse temperature values. Our findings indicate that the results of the hot inner crust substantially influences the mass-radius relationship, resulting in the formation of larger, more inflated neutron stars. A thorough analysis of the hot inner crust is therefore essential for the study of proto-neutron stars.

Key words. Equation of State – Binary merger event – Neutron Stars

1. Introduction

Extensive efforts have been directed towards the dynamical simulations of core-collapse supernovae explosions (Pons et al. 1999; Liebendoerfer et al. 2005; Oertel et al. 2017; Burgio & Fantina (2018) and the subsequent formation and evolution of a proto-neutron star (PNS). A realistic equation of state (EOS) over a wide range of densities of asymmetric nuclear matter is one of the most vital inputs to these calculations (Bethe 1990). Current insights suggest three distinct phases in this process (Pons et al. 1999): (i) Roughly one second post-supernova core bounce, a comparatively cool central region, bordered by a hotter mantle, collapses rapidly, emitting neutrinos while accreting material. (ii) Over the next 20 seconds or so, a slowly developing state of the PNS can be identified, the system first deleptonizes and heats up the interior parts of the star in the process, and then begins to cool down further through neutrino diffusion. (iii) After several minutes, the final state of the neutron star (NS) emerges, cooling initially by neutrino emission and later by photon emission from its surface. Since the composition and physical conditions of the hot newborn PNS (stage (ii)) are quite different from those of a more evolved lepton-poor NS (stage (iii)), in this paper, we focus our attention on the study of the third stage of supernova evolution, considering for simplicity the neutrino-free scenario with an isothermal profile of hot nuclear systems of n , p , e , and μ .

A NS is stratified into three primary regions: the outer crust, the inner crust, and a uniform core. Each region is characterized by distinct physical properties. Within the NS core, matter forms a homogeneous liquid comprising primarily neutrons, augmented by specific fractions of protons, electrons, and muons, ensuring the system remains in β -equilibrium. Deeper within the core, at even greater densities, hyperons, strange baryons, and deconfined quarks can emerge (Shapiro & Teukolsky 1983; Haensel et al. 2007; Anzuini et al. 2021). Transitioning from the core towards the outer layers, the density reduces, causing positive charges to cluster individually, identified by charge Z , and arrange into a solid lattice. This organization minimizes Coulomb repulsion between them. The lattice is embedded in a gas of free neutrons and a background of electrons, ensuring overall charge neutrality for the system. This part is termed the inner crust. Here, nuclear structures may assume non-spherical forms, commonly dubbed 'nuclear pasta', driven by energy minimization (Baym et al. 1971; Lorenz et al. 1993).

In regions of even lower densities, neutrons become sequestered within nuclear clusters, resulting in a lattice structure enriched with neutron-heavy nuclei, interspersed with a degenerate electron gas. This layer is defined as the outer crust (Baym et al. 1971). This crust stretches from the interior, characterized by the neutron drip density, to the exterior, encompassing the envelope layer which plays a pivotal role in NS cooling (Dehman et al. 2023a).

While the core of the star constitutes the majority of its mass and volume, the crust of the NS, despite making up only a small

* Email: c.dehman@csic.es

fraction of its mass and radius, plays a pivotal role in various observable astrophysical phenomena. This significance is evident in phenomena such as bursts and outbursts observed in intensely magnetized NSs, commonly referred to as magnetars (Dehman et al. 2020). To comprehend these bursting mechanisms and harmonize the diverse observations of isolated NSs, magneto-thermal evolution models are indispensable. For an in-depth understanding of the latest magneto-thermal models, we direct the reader to Anzuini et al. (2022); Dehman et al. (2023c,b). The structure of the crust also plays a very important role in the glitch phenomenon in pulsar NS (Piekarewicz et al. 2014).

The inaugural observation of the NS merger event, GW170817, by LIGO-Virgo (LIGO & Virgo 2017) has opened new avenues to study the properties of matter under extreme conditions of density and temperature (Baiotti 2019). Spawned by the confluence of two NSs, these extreme conditions epitomize a transitional phase leading to either a black hole collapse or the genesis of a notably massive NS. It's worth noting that the ultimate outcome of the GW170817 merger remains a subject of ongoing debate.

The zero-temperature EOS imparts a distinct signature on the gravitational waves (GW) signal during the inspiral (pre-merger) phase. This signature becomes evident in the early stages of binary dynamics due to the tidal deformation of the participating stars (Flanagan & Hinderer 2008; Hinderer et al. 2010; Shibata 2015; Krastev & Li 2019). During the post-merger phase, shock heating is anticipated to elevate the remnant's temperature to tens of MeV. Consequently, post-merger characteristics, including the remnant's lifetime, the GW spectrum, and the amounts of mass ejection, are significantly influenced by the finite-temperature EOS (Oechslin, R. et al. 2007; Sekiguchi et al. 2011; Bauswein et al. 2013; Soma & Bandyopadhyay 2020). Advancements in GW detector technology have enabled the imposition of new constraints on the EOS of hot dense matter, serving as pivotal inputs for post-merger numerical simulations. The finite-temperature EOS is instrumental in modeling astrophysical phenomena related to compact objects, such as core-collapse supernovae and the formation of PNSs (Oertel et al. 2017; Kumar et al. 2020). While extensive efforts have been directed towards constructing the EOS for cold-dense matter, the self-consistent finite-temperature EOSs have received comparatively limited attention.

The primary aim of this work is to introduce a suitable method to examine thermal effects on the BCPM (Barcelona-Catania-Paris-Madrid) EOS for nuclear matter in β -equilibrium. Our emphasis lies on the significant impact of the hot inner crust. This thermal EOS is pertinent for compact objects in warm environments such as the aftermath of NS binary mergers (Bethe 1990).

This paper is organised as follows. §2 delves into the BCPM EOS. §2.1 and §2.2 detail the EOS at zero and finite temperatures, respectively. The results obtained in this study are illustrated in §3. We compare our results with observational data and we highlight the important influence of the hot inner crust.

2. BCPM and Equation of State of a β stable matter

2.1. Equation of State at Zero Temperature

Brueckner-Hartree-Fock (BHF) calculations can be directly used to obtain the EOS of the liquid core of NSs, where the nuclei have dissolved into their constituent protons and neutrons. However, a fully microscopic description of finite nuclei and nuclear structures in a NS's crust is not feasible. Density functional the-

ory is currently the only tractable framework for solving the nuclear many-body problem in finite nuclei across the entire nuclear chart. To describe finite nuclei, the BCPM nuclear energy density functional was developed (Baldo et al. 2008; Baldo et al. 2013). Originally designed to characterize the ground state of finite nuclei, this functional was inspired within the Kohn-Sham formulation of density functional theory (Kohn & Sham 1965). It comprises a bulk component, which is derived from the microscopic many-body results for symmetric and neutron matter through local density approximation, along with a phenomenological surface, spin-orbit, Coulomb, and pairing contributions (Baldo et al. 2008; Baldo et al. 2013). The bulk component of the model is obtained using the BHF approach, derived from the bare nucleon-nucleon (NN) interaction in free space, specifically the Argonne v_{18} potential, with the inclusion of three-body forces (TBFs) reduced to a two-body density-dependent term (Wiringa et al. 1995; Taranto et al. 2013). The TBFs, based on the Urbana model, consist of an attractive term resulting from two-pion exchange and a repulsive phenomenological central term designed to replicate the saturation point. The resulting nuclear EOS for both symmetric and asymmetric nuclear matter satisfies several criteria set by heavy ion collisions and astrophysical observations.

We define the total energy per particle as the sum of the kinetic energy per particle, denoted as e_{kin} , and the potential energy per particle, denoted as v_{int} :

$$e(n, \beta) = e_{kin}(n, \beta) + v_{int}(n, \beta). \quad (1)$$

The kinetic energy per particle corresponds to that of a non-interacting Fermi gas with a degeneracy factor g and an isospin asymmetry β :

$$e_{kin}(n, \beta) = \frac{1}{2} \frac{3}{5} \frac{\hbar^2}{2m} \left(\frac{3\pi^2 n}{2} \right)^{2/3} \left[(1 + \beta)^{5/3} + (1 - \beta)^{5/3} \right], \quad (2)$$

with $n = n_n + n_p$ and $\beta = (n_n - n_p)/n$.

The potential energy per particle in the bulk, $v_{int}(n, \beta)$, is represented as a quadratic interpolation between the interaction energy per particle in symmetric nuclear matter (SNM) $v_{int}(n, 0)$ and pure neutron matter (PNM) $v_{int}(n, 1)$:

$$v_{int}(n, \beta) = v_{int}(n, 0) + (v_{int}(n, 1) - v_{int}(n, 0)) \beta^2. \quad (3)$$

The BCPM functional was employed in Sharma et al. (2015) to establish a unified EOS for cold NS. Many-body calculations of the inhomogeneous structures in the NS crust currently fall beyond the scope of the BHF approach, which we use for modeling the homogeneous core. To maintain a consistent microscopic approach for describing the entire stellar structure, we utilize the BCPM functional in the NS crust as well. The NS crust is modeled within the Wigner-Seitz (WS) cell approximation, dividing space into non-interacting cells, each containing a single nuclear cluster in charge and β -equilibrium. In the outer crust, matter is composed of fully ionized atomic nuclei, forming a solid body-centered cubic lattice to minimize Coulomb repulsion, permeated by a degenerated electron gas. The critical data for constructing the outer crust EOS are the nuclear masses, sourced from the AME2012 evaluation (Audi et al. 2012), or, if they are unknown, calculated using the Hartree-Fock-Bogoliubov (HFB) method with the BCPM energy density functional (Sharma et al. 2015). As the star's average density increases, nuclei become increasingly neutron-rich, eventually leading to the inner crust, where neutrons begin to drip. The inner crust thus consists of nuclear clusters immersed in a sea of free neutrons and a background of electrons. In the deepest layers of the inner crust, close

to the transition to the uniform core, nuclear clusters can adopt non-spherical geometries, often referred to as pasta phases.

The complete quantal calculation of the inner crust presents a challenging task due to the presence of neutron gas and the possible existence of non-spherical geometries. To describe the inner crust, we perform self-consistent Thomas-Fermi (TF) calculations with BCPM. This approach offers two significant advantages. On one hand, the EOS in the inner crust is primarily influenced by the neutron gas, which means that shell and pairing effects have a relatively marginal impact. On the other hand, semi-classical methods, as long as they do not incorporate shell effects, are well-suited for describing non-spherical shapes. For a given baryon density and an assumed size R_c of the cell, we conduct a self-consistent TF calculation following the method described in Sharma et al. (2015). This method provides the composition (A, Z) of minimal energy corresponding to the prescribed n_B and R_c values while satisfying β -equilibrium. Subsequently, we search for the optimal cell size for the given baryon density n_B by repeating the calculation with different values of R_c . It's essential to emphasize that this calculation is a very delicate task from the numerical point of view. This sensitivity arises because the energy minimum as a function of R_c is typically extremely flat, and the differences in the total energies involved are often on the order of a fraction of a few keV and sometimes as low as a few eV. It is worth noting that at zero temperature, various shapes of elementary cells in the lattice were explored to identify the most favorable structure. Notably, the presence of the pasta phase was observed at baryon densities very close to the crust-core transition point (Sharma et al. 2015).

Using this formalism, the inner crust, characterized by a low-density neutron gas, and the bulk matter, which comprises high-density nuclear structures, are both determined through BCPM energy density functional. For computational efficiency, we perform a polynomial fit on top of the microscopic BHF calculation in the core. This fit includes fine-tuning the two parameters of the TBFs to ensure that the saturation point is at $E/A = -16$ MeV with a density of $n_0 = 0.16 \text{ fm}^{-3}$. This fit remains valid up to a density of approximately $n \approx 0.4 - 0.5 \text{ fm}^{-3}$. For higher density values, we utilize functional forms that provide excellent parametrizations of the BHF results for SNM and PNM at $T = 0$ (Burgio & J. Schulze 2010):

$$e(n, \beta = 1) = 11n + 309n^{1.95} + 6, \quad (4)$$

and

$$e(n, \beta = 0) = -137n + 308n^{1.82} - 5. \quad (5)$$

Here, the energies are expressed in MeV, and the densities are measured in fm^{-3} .

2.2. Equation of State at Finite Temperature

We aim to extend the BCPM nuclear EOS to finite temperature by introducing thermal effects to the kinetic term of the density functional, while keeping the interactions frozen (i.e., $T = 0$). This approach is known as the frozen correlation approximation, as we assume temperature's effects on interactions to be irrelevant for our study. This approach is checked by comparing our results with the core EOS reported in Lu et al. (2019), where they explored the properties of hot beta-stable matter using EOSs derived within the BHF approach at finite temperature, including consistent TBFs. Our findings are compatible, indicating that the frozen correlation approximation does not introduce a significant error.

2.2.1. The Liquid Core

To determine the self-consistent occupation properties in asymmetric nuclear matter at a temperature T within the non-relativistic mean-field approximation, we minimize the thermodynamic potential, given by:

$$\begin{aligned} G &= \sum_{q=p,n} \sum_k E_q(n_n(k), n_p(k)) - TS - \mu \sum_{q=p,n} \sum_k n_q(k) \\ &= \sum_{q=p,n} \sum_k F_q(n_n(k), n_p(k)) - \mu \sum_{q=p,n} \sum_k n_q(k). \end{aligned} \quad (6)$$

Here, E represents the internal energy, F is the internal free energy, S is the entropy, μ is the chemical potential, and N denotes the number of nucleons in the system.

The total entropy per particle for asymmetric nuclear matter with proton and neutron fraction $y_q = n_q/n$ at finite temperature is expressed as:

$$s(n, \beta, T) = \sum_{q=p,n} y_q s_q(n, \beta, T). \quad (7)$$

Here, s_q represents the entropy per particle of each component:

$$s_q(n, \beta, T) = - \sum_k (n_q(k) \ln n_q(k) + [1 - n_q(k)] \ln [1 - n_q(k)]). \quad (8)$$

In eqs. (6) and (8), $n_q(k)$ are the Fermi occupation numbers, which are the solutions of the variational equations obtained by applying the variational principle to the grand potential (eq. (6)). These occupation numbers read

$$n_q(k) = \frac{1}{1 + e^{(\varepsilon_q(k) - \mu) / T}}, \quad (9)$$

where $q = p, n$, T is the temperature, μ is the chemical potential, and $\varepsilon_q(k)$ is the single-particle spectrum defined as:

$$\varepsilon_q(k) = \frac{\hbar^2 k^2}{2m} + V_q(n, \beta), \quad (10)$$

with V_q in the frozen correlation approximation being a constant that depends solely on the density and is given by:

$$\begin{aligned} V_q(n, \beta) &= \frac{\partial(n v_{int}(n, \beta))}{\partial n_q}, \\ &= v_{int}(n, \beta) + n \frac{\partial v_{int}(n, \beta)}{\partial n_q}. \end{aligned} \quad (11)$$

The density n_q of neutrons and protons is given by:

$$n_q = \frac{g}{(2\pi)^3} \int_0^\infty n_q(k) d^3k = \frac{g}{4\pi^2} \left(\frac{2mT}{\hbar^2} \right)^{3/2} J_{1/2}(\eta_q) \quad (12)$$

where the factor 2 corresponds to the spin degeneracy of protons and neutrons, and $J_{1/2}(\eta_q)$ is the Fermi integral for index $\nu = 1/2$. The Fermi integrals for an arbitrary index ν are defined as: and $J_{1/2}(\eta_q)$ is the Fermi integral:

$$J_{1/2}(\nu_q) = \int_0^\infty \frac{z^{1/2} dz}{1 + e^{z - \eta_q}}, \quad (13)$$

where $z = [\varepsilon_q(k) - V_q] / T$ and the fugacity reads $\eta_q = [\mu_q - V_q] / T$.

At finite temperature, we define the total energy per particle as:

$$e(n, \beta, T) = e_{\text{kin}}(n, \beta, T) + v_{\text{int}}(n, \beta). \quad (14)$$

The interaction term, denoted as $v_{int}(n, \beta)$, which is a function of the neutron and proton number densities only, remains the same at both zero and finite temperature owing to the frozen correlations approximation, and it is defined in eq. (3).

The kinetic energy per particle is that of a non-interacting Fermi gas:

$$e_{kin}(n, \beta, T) = \frac{\hbar^2}{2m} \frac{\sum_{q,l} \tau_q}{n}, \quad (15)$$

where $q = n, p$ and $l = e, \mu$. The term τ_q is defined as:

$$\tau_q = \frac{g}{4\pi^2} \left(\frac{2mT}{\hbar^2} \right)^{5/2} J_{3/2}(\eta_q), \quad (16)$$

with $J_{3/2}(\eta_q)$ being the Fermi integral of index $\nu = 3/2$.

$$J_{3/2}(\eta_q) = \int_0^\infty \frac{z^{3/2} dz}{1 + e^{z - \eta_q}}. \quad (17)$$

In our approach, nucleons are treated as non-relativistic particles, while the leptons are considered as relativistic free particles. The contribution of leptons to the energy per baryon is given by:

$$e_l = \frac{1}{A} \int_0^{k_{Fl}} \frac{k^2 dk}{\pi^2} \sqrt{\hbar^2 k^2 c^2 + m_l^2 c^4}. \quad (18)$$

Here, $k_{Fl} = (3\pi^2 n_l)^{1/3}$ represents the lepton Fermi wave-number, and $l = e, \mu$.

The proton and neutron chemical potentials can be expressed in terms of temperature T , fugacity η_q , and the interacting part of the chemical potential, which, in our case, remains the same as at zero temperature:

$$\mu_q(n, \beta, T) = \eta_q T + V_q(n, \beta). \quad (19)$$

For stellar matter containing nucleons and leptons as relevant degrees of freedom, the chemical equilibrium conditions are:

$$\mu_n - \mu_p = \mu_e = \mu_\mu. \quad (20)$$

The pressure is given by:

$$P(n, \beta, T) = n \left[\sum_{q=p,n} y_q \mu_q(n, \beta, T) - f(n, \beta, T) \right]. \quad (21)$$

2.2.2. The Hot Inner Crust

The TF method has been applied at finite temperature to calculate the structure and EOS of the crust using the BCPM model. In the inner crust, nuclear clusters are assumed to arrange in a body-centered cubic lattice, approximated as spherical WS cells with a radius of R_c . Each WS cell is electrically neutral, and interactions between cells are neglected. At nuclear densities, the Fermi momenta of the electrons are much larger than their rest mass, making them highly relativistic. Therefore, they can be assumed to be uniformly distributed within the WS cell. Inside the WS cell, we assume β -equilibrium, leading to the condition $\mu_n = \mu_p + \mu_e$ when neutrinos have left the star. Similar to the core, the properties of the system of neutrons, protons, and electrons at finite temperature within a WS cell of volume V_c are determined by minimizing the thermodynamic potential (eq. (6)), which in the case of the crust also includes non-uniform contributions (see below). It's important to note that at higher temperatures, nuclei become unstable against nucleon evaporation. Thus, within the WS cell, a coexistence between the nuclear cluster plus gas and

the gas alone, occurs. Thus, the TF approach at finite temperature in a WS cell is based on the existence of two solutions of the TF equations: one corresponding to the liquid plus gas phase (LG) and the other corresponding to the gas phase alone (G).

In the context of the crust, the internal energy contributing to the thermodynamic potential is expressed as:

$$E = \int_{V_c} dV \left[\mathcal{H}(n_n, n_p) + \mathcal{E}_{el} + \mathcal{E}_{coul} + \mathcal{E}_{ex} + m_p n_p + m_n n_n \right]. \quad (22)$$

Here, $\mathcal{H}(n_n, n_p)$ represents the nuclear energy density, with n_n and n_p denoting the neutron and proton number densities, respectively. In the hot TF approach, \mathcal{H} incorporates the kinetic energy density of protons and neutrons at finite temperature (see eq. (15)). Additionally, it includes the cold interacting part $\mathcal{V}(n_n, n_p)$, as determined by the BCPM functional, which encompasses bulk (eq. (3)) and surface contributions. The surface term is considered at zero temperature and is defined as:

$$\begin{aligned} \mathcal{E}_{surf}(n, \beta) &= \frac{1}{2} \sum_{q,q'} n_q(\mathbf{r}) \int v_{q,q'}(\mathbf{r} - \mathbf{r}') n_{q'}(\mathbf{r}') d\mathbf{r}' \\ &\quad - \frac{1}{2} \sum_{q,q'} n_q(\mathbf{r}) n_{q'}(\mathbf{r}') \int v_{q,q'} \mathbf{r}' d\mathbf{r}'. \end{aligned} \quad (23)$$

The second term in eq. (23) is subtracted to avoid affecting the bulk part derived from microscopic nuclear matter calculations. For finite-range form factors, we employ a Gaussian shape $v_{q,q'}(\mathbf{r}) = V_{q,q'} e^{-r^2/\alpha^2}$ with three adjustable parameters, including the range α , the strength $V_{p,p} = V_{n,n} = V_L$ for like nucleons, and the strength $V_{n,p} = V_{p,n} = V_U$ for unlike nucleons. The term \mathcal{E}_{el} represents the energy density arising from the motion of electrons at finite temperature, with their kinetic energy per particle given in eq. (18).

At finite temperature, the direct Coulomb contribution in a WS cell corresponding to the LG and G phases, as discussed in Sil et al. (2002), is given by:

$$\mathcal{E}_{LG}(n_p, n_e) = \frac{1}{2} (n_{LG}^p(\mathbf{r}) - n_e) (V_{LG}^p(\mathbf{r}) - V_e(\mathbf{r})), \quad (24)$$

and

$$\begin{aligned} \mathcal{E}_G(n_p, n_e) &= \frac{1}{2} (n_G^p(\mathbf{r}) - n_e) (V_G^p(\mathbf{r}) - V_e(\mathbf{r})) \\ &\quad + n_L^p(\mathbf{r}) (V_G^p(\mathbf{r}) - V_e(\mathbf{r})), \end{aligned} \quad (25)$$

where $n_L^p = n_{LG}^p - n_G^p$ is the proton density of the nuclear cluster in the subtracted picture. The potentials $V_{LG(G)}^p(\mathbf{r})$ are calculated using the following equations:

$$V_{LG(G)}^p(\mathbf{r}) = \int \frac{e^2 n_{LG(G)}^p(\mathbf{r}')}{|\mathbf{r} - \mathbf{r}'|} d\mathbf{r}', \quad V_e(\mathbf{r}) = \int \frac{e^2 n_e}{|\mathbf{r} - \mathbf{r}'|} d\mathbf{r}'. \quad (26)$$

The direct part of the single-particle Coulomb potential, obtained by performing the functional derivatives of the LG and G direct Coulomb energies with respect to n_{LG} and n_G , respectively, is the same for both phases. It is given by:

$$V_c^d(\mathbf{r}) = \int \frac{e^2 (n_{LG}^p(\mathbf{r}') - n_e)}{|\mathbf{r} - \mathbf{r}'|} d\mathbf{r}', \quad (27)$$

The total Coulomb energy in the LG and G phases is composed of the direct contributions, as described in eqs. (24) and (25), respectively, plus the exchange contribution from protons

and electrons, which is calculated at the Slater level. The latter is given by:

$$\mathcal{E}_{LG(G)}^{ex}(n_{LG(G)}^p, n_e) = -\frac{3}{4}\left(\frac{3}{\pi}\right)^{1/3} e^2 (n_{LG(G)}^p)^{4/3} + n_e^{4/3}. \quad (28)$$

Taking functional derivatives of the thermodynamical potential (eq. (6)) with the energy density given by eq. (22), which includes Coulomb effects in both LG and G phases, with respect to n_{LG}^q and n_G^q for neutrons and protons, we obtain the following set of coupled equations, as described in Sil et al. (2002):

$$T\eta_{LG}^q(\mathbf{r}) + V_{LG}^q(\mathbf{r}) + V_{LG}^{coul}(\mathbf{r}) = \mu_q, \quad (29)$$

$$T\eta_{LG}^q(\mathbf{r}) + V_G^q(\mathbf{r}) + V_G^{coul}(\mathbf{r}) = \mu_q, \quad (30)$$

where $V_{LG(G)}^q$ represents the nuclear part of the single-particle potential in the LG(G) phases, and $V_{LG(G)}^{coul}$ is the total Coulomb potential, comprising the direct term from eq. (27) and the exchange part obtained from derivatives with respect to n_{LG}^p (n_G^p) of the exchange energy as given in eq. (28).

For a given baryon density n_B and an assumed size of R_c for the cell, the set of variational equations is solved numerically and self-consistently, following the method described in Sil et al. (2002), which allows to determine the composition (A, Z) of minimal energy in β -equilibrium. Next, we search for the optimal cell size for the given baryon density n_B by repeating the calculation for various values of R_c . In our study, at finite temperature, we assume only spherical droplet configurations in the WS cells. This choice is motivated by the following reasons: i) The computation is a delicate numerical task because the energy minimum is often relatively flat as a function of the cell radius R_c , or equivalently, as a function of the baryon number A . The energy differences can be on the order of a few keV to a few eV. ii) At $T=0$, non-spherical shapes appear in a very small density region near the core, typically within a range like $[0.078:0.08] \text{ fm}^{-3}$, as indicated in Fig. 4 of Sharma et al. (2015). Additionally, the crust-core transition density shifts to lower densities at finite temperatures. Therefore, for simplicity, we assume only spherical droplet WS cells. It's worth noting that different geometrical shapes do not have a significant impact on the EOS, such as pressure and density.

We are focused on calculating the exact EOS in various regions of the NS, with a specific emphasis on determining the structure and EOS in the crust using the BCPM model at a finite temperature. To obtain the EOS in the inner crust, it is necessary to compute the pressure. The pressure in the inner crust is a result of the neutron and electron gases within which the nuclear structures are embedded. The pressure is determined by taking appropriate derivatives of the energy with respect to the size of the WS cell. For a more detailed explanation, we direct the reader to Appendix A of Sharma et al. (2015). The resulting expression for the pressure is as follows:

$$P = P_{ng} + P_{free}^{el} + P_{ex}^{el}. \quad (31)$$

Here, P_{ng} represents the pressure exerted by the gas of dripped neutrons, P_{free}^{el} is the pressure contributed by the free electron gas, and $P_{ex}^{el} = \frac{1}{3}\mathcal{E}_{ex}^{el}$ accounts for a correction stemming from electron Coulomb exchange.

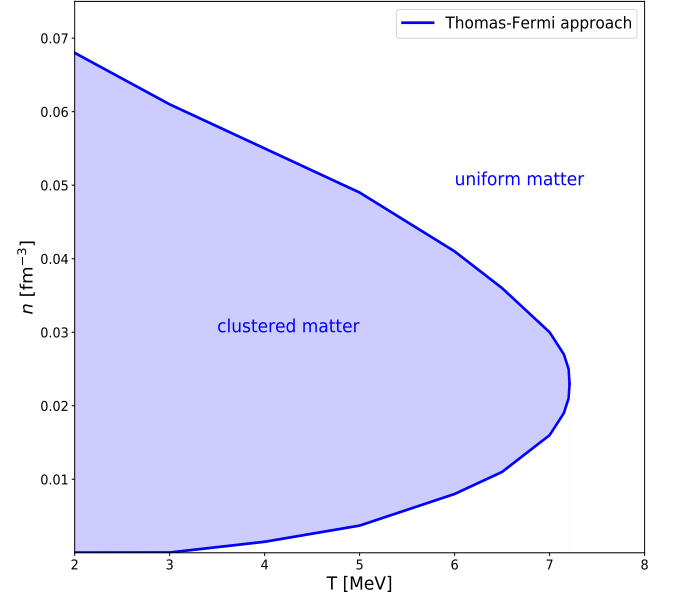


Fig. 1. The two branches, upper and lower, of the transition density between the uniform matter and the clusters are computed at different temperature values. The blue shaded area corresponds to the presence of nuclear clusters, which were computed using TF calculations within a WS cell.

3. Impact of Hot Crust

To study the EOS in the NS crust at finite temperatures, it is essential to examine the transition between crust and uniform matter across different temperature ranges. This is a complex and lengthy process. Although it is possible to find the transition density from the core (or uniform matter) side, here we search the transition density from the crust's perspective in order to highlight the behaviour of the crust at finite temperature and its transition to the core.

From the crust side, at finite temperature by searching for the configuration, which includes the nuclear composition and the size of the WS cell, by means of the hot TF method discussed in the previous section. We then compare this energy value with the one predicted by uniform matter at the same density and asymmetry. The energy per baryon within a WS cell is computed using the TF approach at finite temperature discussed in the previous section.

Table 1. Table showing the upper (n_t^u) and lower (n_t^l) transition densities as illustrated in Fig. 1 for specific temperature values.

T (MeV)	n_t^u (fm^{-3})	n_t^l (fm^{-3})
2.00	0.068	3×10^{-5}
3.00	0.061	0.0004
4.00	0.055	0.0015
5.00	0.049	0.0037
6.00	0.041	0.008
6.50	0.036	0.011
7.00	0.030	0.016
7.15	0.027	0.019
7.20	0.025	0.021
7.21	0.023	0.023

In Fig. 1, we present the boundary of crust-uniform matter transition densities as a function of temperature, derived from TF

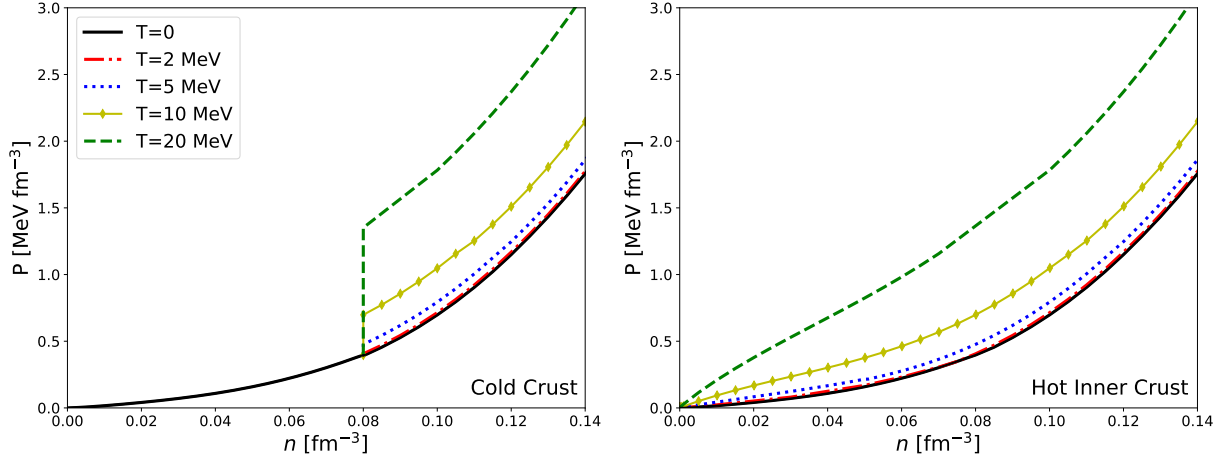


Fig. 2. EOSs at different temperature values, e.g., $T = 0, 5, 10, 15$, and 20 MeV. In the left panel, we use a cold crust assuming the connection between the cold crust and the uniform core at $n = 0.08 \text{ fm}^{-3}$. In the right panel, we use a hot inner crust, the outer–inner crust transition density is fixed to 10^{-4} fm^{-3} and the crust–core transition density is fixed as described in §2.

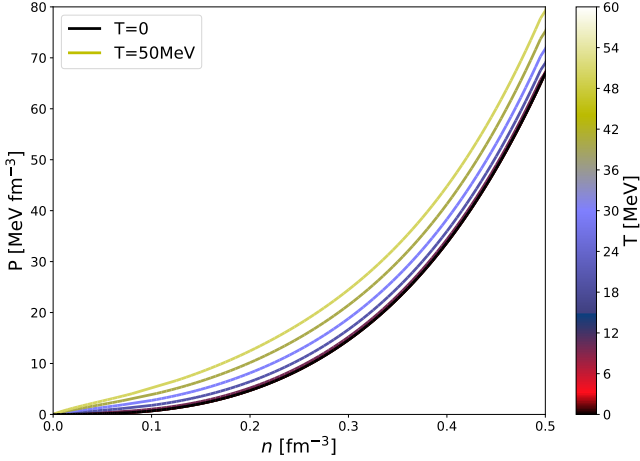


Fig. 3. EOSs at different temperature values from $T = 0$ to 50 MeV. For $T = 0, 2$, and 5 MeV, we display the exact NS EOS containing the hot crust using BCPM. Above $T > 7.2$ MeV, the NS is made of homogeneous dense matter, thus we illustrate the results of the bulk part of BCPM.

calculations. This figure features a thick blue line in the density–temperature plane that delineates two regions: outside the curve, where uniform matter is the most stable phase, and inside the curve, where clusterized matter is more stable. The figure also illustrates that the crust–uniform matter transition boundary, as a function of temperature, is a bivalued function that decreases with increasing temperature until it converges to a single endpoint. This endpoint occurs at a specific limiting temperature (T_{lim}), beyond which crust–uniform matter transitions are not feasible. The upper and lower transition densities illustrated in Fig. 1 for some specific temperature values are collected in Table 1.

At zero temperature, the inner crust of a NS is composed of nuclear clusters that encapsulate all the protons present in the WS cell, surrounded by a gas of dripped neutrons. Within the WS framework, as the average density rises, the contribution from the neutron gas also increases. The crust–core transition is decided by an energy criterion, the phase transition takes place when the energy of the homogeneous phase is lower than in the clustered phase. It is crucial to note that at non-zero tempera-

tures, neutrons evaporate from the cluster into the surrounding gas, resulting in an increased neutron number in the gas phase. Protons also evaporate, but at a slower rate compared to neutrons. This fact has, however, important consequences. At zero temperature, clustered matter represents the most stable phase for any density below the transition density. However, at finite temperatures, a lower threshold density exists, below which uniform matter becomes the most stable phase. As depicted in Fig. 1, the density range at a given temperature in which clustered matter is the most stable phase diminishes with increasing temperature. The upper and lower boundaries defining this region converge, ultimately merging into a single point at the limiting temperature. This scenario is akin to the phenomena observed in nuclear matter when analyzing instabilities within a homogeneous medium (Barranco & Buchler 1981; Lattimer & Swesty 1991; Hempel & Schaffner-Bielich 2010).

It is noteworthy that at the transition density between the crust and uniform matter for both branches, our findings indicate that the proton fraction at these points is approximately 0.03 . Furthermore, the proton fraction maintains a relatively stable value across all transition densities. Additionally, we have computed the plasma parameter, defined as $\Gamma = (Z_{\text{cl}}e)^2/(R_c T)$, at the transition density points illustrated in Table 1 and Fig. 1. We find that Γ is consistently less than 175 at all transition densities, indicating that the clusters are in the liquid phase (Pi et al. 1986). These results are in agreement with the literature (Aguilera et al. 2008).

In the literature, certain studies of the NS EOS at finite temperatures assume that thermal effects in the crust are negligible. Consequently, their EOSs are composed of a hot core starting from a specified value of the core–crust transition density computed at zero temperature, supplemented by a cold crust contribution obtained from existing literature (Lu et al. 2019). In the left panel of Fig. 2, we illustrate this type of NS EOSs using the BCPM density functional at various temperatures, including $T = 0, 2, 5, 10$, and 20 MeV, while considering a cold crust. In this case, we have maintained the zero-temperature density transition point between the inner crust and the core at $n(T = 0) = 0.08 \text{ fm}^{-3}$, as reported in Sharma et al. (2015). For temperatures $T \leq 2$ MeV, the discontinuity between the cold crust and the hot core EOS is acceptable. However, as the temperature increases, e.g., $T = 5, 10, 15, 20$ MeV, the discontinuity becomes more and more pronounced.

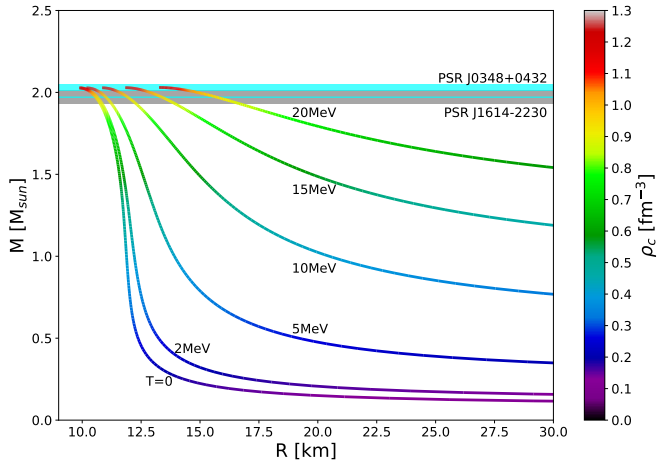


Fig. 4. Mass–radius relations for neutrino free matter considering an isothermal profile of NSs at $T = 0, 2, 5, 15$ and 20 MeV. The observational constraints are $1.97 \pm 0.04 M_{\text{sun}}$ (gray band) from the PSR J1614-2230 pulsar (Demorest et al. 2010) and $2.01 \pm 0.04 M_{\text{sun}}$ (cyan band) from the PSR J0348+0432 pulsar (Antoniadis et al. 2013).

We compute the crust EOS at $T = 2$ MeV and $T = 5$ MeV, and we assume that the NS is made of a homogeneous dense material without a clustered inner crust for $T > 7.2$ MeV. When a constant temperature is assumed (isothermal profile), the radius of the star cannot be defined by the usual condition of vanishing pressure if a complete hot isothermal crust is assumed. This is because at finite temperature, the pressure does not vanish, even at very low densities, and, consequently, the thermal effect causes isolated NSs to expand. To address this, a temperature drop from the interior to the surface of the star is necessary. Various alternatives have been explored in the literature, such as using a neutrino-sphere to ensure the temperature drops to zero at low density (Gondek et al. 1997), or adopting a fixed entropy approach in the outer crust (Burgio et al. 2011). For this reason, we have coupled in our study the finite temperature EOSs with the EOS of the cold outer crust to obtain a cold surface. In regions of very low density, $n < 10^{-4} \text{ fm}^{-3}$, a cold outer crust is employed to guarantee that the pressure decreases to extremely low values. The rationale for selecting the value of 10^{-4} fm^{-3} which agrees with the outer to inner crust transition density of the BCPM model at $T = 0$.

For temperatures below 7.2 MeV, we employ the results obtained in Fig. 1 and Table 1. When the temperature exceeds 7.2 MeV, the hot inner crust ceases to exist; consequently, we utilize hot uniform matter calculations throughout. For all temperature values, we rely on the cold outer crust for densities below 10^{-4} fm^{-3} . It's worth noting that when considering the cold outer crust, our results align with those obtained by Gondek et al. (1997), who adopted the neutrino-sphere approach for an isothermal NS profile at $T = 15$ MeV.

Plots of the EOSs at different temperatures with the hot inner crust prescription are depicted in the right panel of Fig. 2 and in Fig. 3. In the latter, we plot a wider range of EOSs at finite temperatures, extending up to $T=50$ MeV. A consistent trend of growth is observed for all temperatures.

The mass-radius relations of neutrino-free β -stable matter, considering an isothermal profile, are illustrated in Fig. 4 at different temperature values. For the sake of comparison, we also show the cold NS models at $T = 0$. The color-bar reflects the central density. The values of the masses used to depict the constraint of $M \sim 2 M_{\text{sun}}$ in the M–R graph are $1.97 \pm 0.04 M_{\text{sun}}$

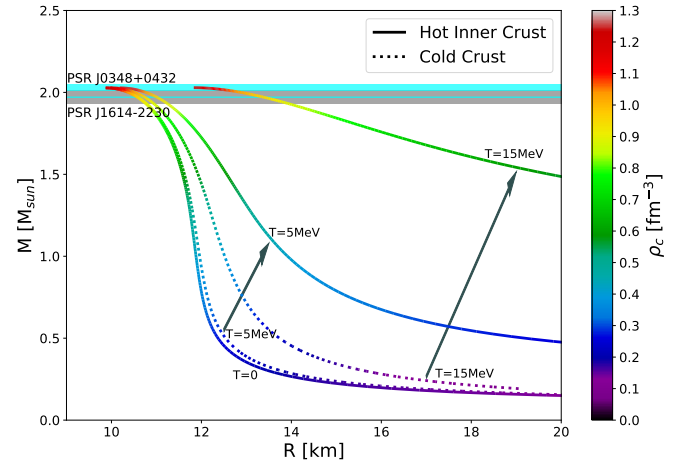


Fig. 5. Mass–radius relations for neutrino-free matter considering an isothermal profile of NSs at $T = 0, 5, 15$ MeV. The dotted lines correspond to EOSs with cold crust and the solid lines correspond to EOSs with hot crust (same as Fig. 4). Note that the horizontal scale goes up to 20 km, whereas in Fig. 4 it goes up to 30 km. The observational constraints are $1.97 \pm 0.04 M_{\text{sun}}$ (gray band) from the PSR J1614-2230 pulsar Demorest et al. (2010) and $2.01 \pm 0.04 M_{\text{sun}}$ (cyan band) from the PSR J0348+0432 pulsar Antoniadis et al. (2013). The two arrows indicate the shift in the mass–radius relation for $T=5$ and $T=15$ MeV.

from the PSR J1614-2230 pulsar (Demorest et al. 2010) and $2.01 \pm 0.04 M_{\text{sun}}$ from the PSR J0348+0432 pulsar (Antoniadis et al. 2013). The two observational limits are displayed with gray and cyan bands, respectively. The maximum mass M_{max} of a NS slightly increases when temperature grows, compared to the cold $T = 0$ case, but it remains below the observed upper limit set by the PSR J0348+0432 pulsar (Antoniadis et al. 2013). The radius of the NS corresponding to the maximum mass shifts towards a larger value when the temperature increases. Furthermore, as it can be seen from the colorbar, the highest central density value, which corresponds to the maximum mass, decreases as the NS mass decreases and the NS radius increases. It is worth mentioning that we have compared our results of the mass-radius relation with those from Gondek et al. (1997), which were obtained by considering an isothermal temperature profile at $T = 15$ MeV and a neutrino-sphere, instead of a cold outer crust. We found that our results are consistent with their findings.

To emphasize the impact of the hot inner crust, we present a comparison of the mass-radius relations in Fig. 5. On one hand, we consider a full cold crust (dotted lines), and on the other hand, a hot inner crust (solid lines) at $T=5$ and 15 MeV. We also include the mass-radius relation at $T=0$ as a reference. The two arrows indicate the shift in the mass-radius relation for $T=5$ and $T=15$ MeV when the hot crust is considered. The EOSs with a cold crust predict mass-radius relations that are similar to those at $T=0$, particularly for low temperature values, e.g., $T = 5$ MeV, and around the maximum mass, i.e., $M \sim 2 M_{\text{sun}}$. However, when considering a hot inner crust, the effect of the temperature on the mass-radius relation becomes much more relevant. Comparing the central densities predicted by considering a full cold crust and a hot inner crust (see Fig. 5), we notice that for a given NS radius, the central density is shifted to larger values when the hot crust is considered. Therefore, the hot inner crust significantly modifies the mass-radius relation with respect to the full cold crust. Thus, using the calculation of cold crust for a density below 0.08 fm^{-3} is not the best realistic scenario.

Additionally, we have compared our results of the cold crust at $T=5$ and 15 MeV with those of Lu et al. (2019), where they consider a non-frozen correlation approximation in their study. We find that our results are consistent with those of Lu et al. (2019). Thus, we expect that the frozen correlation approximation does not have a substantial impact on our results.

4. Conclusion

We have investigated the properties of stellar matter at finite temperature by means of the thermal BCPM energy density functional. To this end, we introduce the thermal effects only in the kinetic term of the energy density functional, while keeping the interactions fixed at zero temperature, which corresponds to the frozen approximation. As a consequence, the EOS corresponding to the core is obtained using the hot HF method, which is explained in detail in subsection. To determine the EOSs of the hot crust across different temperature values, we perform self-consistent TF calculations using the BCPM energy density functional, considering spherical droplets configurations in the WS approximation. This hot EOS is complemented by the cold BCPM EOS for the outer crust which extends up to a density of 10^{-4} fm^{-3} . This is done in order to get vanishing pressure at the surface of the star.

We find that the inner crustal region, as predicted from the TF calculations, completely dissolves at temperatures exceeding 7.2 MeV for our BCPM EOS, a point also referred to as the limiting temperature. This results in the entire star being pervaded by hot, homogeneous, and dense matter. Above this limiting temperature, the NS consists entirely of uniform matter at densities greater than that corresponding to the border of the cold outer crust (10^{-4} fm^{-3}).

Our analysis of the hot inner crust has revealed two distinct branches of transition density between uniform and clustered matter. The branch with a higher density value represents the upper transition density, which delineates the transition between the inner crust and the core that is similar to the crust-core transition at zero temperature. Conversely, the branch with a lower density value indicates another lower transition density, suggesting the re-emergence of uniform matter in the NS's outer layer. This second crust-uniform matter transition, does not appear at zero temperature. Observe that at a finite temperature, the presence of evaporated protons in the gas phase, which is in equilibrium with the liquid-gas phase, causes the energy per baryon in the cluster within the inner crust to be higher than the energy per baryon in uniform matter at the same average density and in beta-equilibrium. However, this is not the case at zero temperature.

We have studied the mass-radius relations at finite temperatures. For our analysis, we utilized observational limits from the PSR J1614-2230 (Demorest et al. 2010) and the PSR J0348+0432 (Antoniadis et al. 2013) pulsars. Our findings indicate that the influence of thermal effects becomes relevant. On the one hand, for a given mass of the NS, its radius increases with temperature and this growing is larger for higher temperatures. On the other hand, for a given radius of the NS, its mass also increases with temperature, but saturating to a value close to the maximum mass of cold NS for large enough temperature. Furthermore, when comparing our findings to results obtained with a cold crust, we observed that the impact on the mass-radius relation is significant. From Figure. 5, we see thermal effects due to the hot core is moderate while the contribution of the hot crust to the mass-radius relationship is much more important. Hence, for

NSs in hot environments, such as the end products of NS merger events, it's essential to accurately address the inner crust.

In this study, we successfully extended the BCPM EOS to finite temperatures within the frozen correlation approximation, ensuring a meticulous treatment of the inner crust. The BCPM energy density functional provides a unified EOS for NSs under both cold and hot conditions. Furthermore, we determined the mass-radius relations and the central densities of hot compact objects at different temperature levels, underscoring the significance of precisely addressing the inner crust.

Acknowledgements. This investigation was initiated in collaboration with Prof. Artur Polls (\dagger 12-08-20), who made significant contributions to this study. We would like to dedicate this work in honor of his memory. CD has the partial support of NORDITA while working on this article and is supported by the ERC Consolidator Grant “MAGNESIA” No. 817661 (PI: Rea). This work is partially supported by the program Unidad de Excelencia María de Maeztu CEX2020-001058-M. We also acknowledge partial support from grant SGR2021-01269 (PI: Graber). MC and XV acknowledge partial support from Grants No. PID2020-118758GB-I00 and No. CEX2019-000918-M (through the “Unit of Excellence María de Maeztu 2020-2023” award to ICCUB) from the Spanish MCIN/AEI/10.13039/501100011033.

References

- Aguilera, D. N., Pons, J. A., & Miralles, J. A. 2008, *A&A*, 486, 255
- Antoniadis, J., Freire, P. C. C., Wex, N., et al. 2013, *Science*, 340, 448
- Anzuini, F., Melatos, A., Dehman, C., Viganò, D., & Pons, J. A. 2021, *MNRAS*, 509, 2609
- Anzuini, F., Melatos, A., Dehman, C., Viganò, D., & Pons, J. A. 2022, *MNRAS*, 515, 3014
- Audi, G., M., W., A. H., W., et al. 2012, *Chinese Physics C*, 36, 002
- Baiotti, L. 2019, *Progress in Particle and Nuclear Physics*, 109, 103714
- Baldo, M., Robledo, L. M., Schuck, P., & Viñas, X. 2013, *Phys. Rev. C*, 87, 064305
- Baldo, M., Schuck, P., & G. Viñas, X. 2008, *Phys. Lett. B*, 663, 390
- Barranco, M. & Buchler, J.-R. 1981, *Phys. Rev. C*, 24, 1191
- Bauswein, A., Baumgarte, T. W., & Janka, H.-T. 2013, *Phys. Rev. Lett.*, 111, 131101
- Baym, G., Bethe, H. A., & Pethick, C. J. 1971, *Nature*, 175, 225
- Baym, G., Pethick, C., & Sutherland, P. 1971, *The Astrophysical Journal*, 170, 299
- Bethe, H. A. 1990, *Rev. Mod. Phys.*, 62, 801
- Burgio, G. F. & Fantina, A. F. (2018), in *The Physics and Astrophysics of Neutron Stars* (Springer), 255
- Burgio, G. F., Ferrari, V., Gualtieri, L., & Schulze, H. J. 2011, *Physical Review D*, 84, 044017
- Burgio, G. F. & J. Schulze, H. 2010, *Astron. Astrophys.*, 518
- Dehman, C., Pons, J. A., Viganó, D., & Rea, N. 2023a, *mnras* [arXiv:2301.02261]
- Dehman, C., Viganó, D., Ascenzi, S., Pons, J. A., & Rea, N. 2023b, *MNRAS*, 523, 5198
- Dehman, C., Viganó, D., Pons, J. A., & Rea, N. 2023c, *mnras*, 518, 1222
- Dehman, C., Viganó, D., Rea, N., et al. 2020, *The Astrophysical Journal Letters*, 902, L32
- Demorest, P. B., Pennucci, T., Ransom, S. M., Roberts, M. S. E., & Hessels, J. W. T. 2010, *Nature*, 467, 1081
- Flanagan, E. E. & Hinderer, T. 2008, *Phys. Rev. D*, 77, 021502
- Gondek, D., Haensel, P., & Zdunik, J. L. 1997, *AAP*, 325, 217
- Haensel, P., Potekhin, A. Y., & Yakovlev, D. G. 2007, *Neutron stars 1: Equation of state and structure*, Vol. 326 (New York, USA: Springer)
- Hempel, M. & Schaffner-Bielich, J. 2010, *Nucl. Phys. A*, 837, 210
- Hinderer, T., Lackey, B. D., Lang, R. N., & Read, J. S. 2010, *Phys. Rev. D*, 81, 123016
- Kohn, W. & Sham, L. J. 1965, *Phys. Rev.*, 140, A1133
- Krastev, P. G. & Li, B. A. 2019, *J. Phys. G: Nucl. and Part. Phys.*, 46, 074001
- Kumar, A., Huded, C. P., Zhou, L., et al. 2020, *The American Journal of Cardiology*, 134, 1
- Lattimer, J. M. & Swesty, D. F. 1991, *Nucl. Phys. A*, 535, 331
- Liebendoerfer, M., Rampp, M., Janka, H. T., & Mezzacappa, A. 2005, *Astrophys. J*, 620, 840
- LIGO & Virgo. 2017, *Phys. Rev. Lett.*, 119, 161101
- Lorenz, C. P., Ravenhall, D. G., & Pethick, C. J. 1993, *Phys. Rev. Lett.*, 70, 379
- Lu, J.-J., Li, Z.-H., Burgio, G. F., Figura, A., & Schulze, H. J. 2019, *Phys. Rev. C*, 100, 054335

- Oechslin, R., Janka, H.-T., & Marek, A. 2007, *A&A*, 467, 395
- Oertel, M., Hempel, M., Klähn, T., & Typel, S. 2017, *Rev. Mod. Phys.*, 89, 015007
- Pi, M., Vinas, X., Barranco, M., Polls, A., & Perez-Canyellas, A. 1986, *A&AS*, 64, 439
- Piekarewicz, J., Fattoyev, F. J., & Horowitz, C. J. 2014, *Phys. Rev. C*, 90, 015803
- Pons, J., Reddy, S., Prakash, M., Lattimer, J., & Miralles, J. 1999, *Astrophys. J.*, 513, 780
- Sekiguchi, Y., Kiuchi, K., Kyutoku, K., & Shibata, M. 2011, *Phys. Rev. Lett.*, 107, 051102
- Shapiro, S. L. & Teukolsky, S. A. 1983, *Black holes, white dwarfs, and neutron stars : the physics of compact objects* (Wiley)
- Sharma, B. K., Centelles, M., Viñas, X., Baldo, M., & Burgio, G. F. 2015, *Astron. Astrophys.*, 584, A103
- Shibata, M. 2015, *Numerical relativity*, Vol. 1 (World Scientific)
- Sil, T., De, J. N., Samaddar, S. K., et al. 2002, *Physical Review C*, 66, 045803
- Soma, S. & Bandyopadhyay, D. 2020, *The Astrophysical Journal*, 890, 139
- Taranto, G., Baldo, M., & Burgio, G. F. 2013, *Phys. Rev. C*, 87, 045803
- Wiringa, R. B., Stoks, V. G. J., & Schiavilla, R. 1995, *Phys. Rev. C*, 51, 38